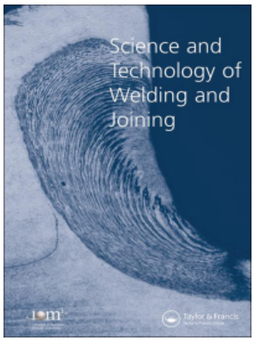

Taylor & Francis
Taylor & Francis Group

Science and Technology of Welding and Joining

ISSN: (Print) (Online) Journal homepage: https://www.tandfonline.com/loi/ystw20

Direct drive friction welding of a multi-phase $Al_{13}Cr_{23.5}Fe_{20}Co_{20}Ni_{23.5}$ high-entropy alloy

Lei Zuo, Kai Zhang & Tao Zhang

To cite this article: Lei Zuo, Kai Zhang & Tao Zhang (2021) Direct drive friction welding of a multi-phase $Al_{13}Cr_{23.5}Fe_{20}Co_{20}Ni_{23.5}$ high-entropy alloy, Science and Technology of Welding and Joining, 26:7, 513-520, DOI: 10.1080/13621718.2021.1957631

To link to this article: https://doi.org/10.1080/13621718.2021.1957631

SCIENCE AND TECHNOLOGY OF WELDING AND JOINING
2021, VOL. 26, NO. 7, 513–520
https://doi.org/10.1080/13621718.2021.1957631

I·M3 Institute of Materials, Minerals & Mining
Taylor & Francis
Taylor & Francis Group

RESEARCH ARTICLE

Direct drive friction welding of a multi-phase $Al_{13}Cr_{23.5}Fe_{20}Co_{20}Ni_{23.5}$ high-entropy alloy

Lei Zuo[a], Kai Zhang[a] and Tao Zhang[b]

[a]School of Aerospace Engineering, Beijing Institute of Technology, Beijing, People's Republic of China; [b]Key Laboratory of Aerospace Materials and Performance (Ministry of Education), School of Materials Science and Engineering, Beihang University, Beijing, People's Republic of China

ABSTRACT

$Al_{13}Cr_{23.5}Fe_{20}Co_{20}Ni_{23.5}$ high-entropy alloy with three phases (face-centered cubic [FCC], A2 and B2) was joined successfully by direct drive friction welding. The microhardness of the welded samples gradually increases as approaching the weld interface, which was related to the microstructural evolution across the weld interface. The weld joint can be divided into four regions: dynamic recrystallisation zone, thermal-mechanically affected zone, heat affected zone and base metal. It is found that the volume fraction ratio of FCC to body-centered cubic (BCC) (A2+B2) phases slightly decreases as approaching the weld interface. The hardening of the joint is attributed to the refined structure, large deformation and the increased volume fraction of the hard BCC phases in the weld joint.

ARTICLE HISTORY
Received 22 April 2021
Revised 6 July 2021
Accepted 8 July 2021

KEYWORDS
High-entropy alloys; mechanical properties; direct-drive friction welding; microstructure

Introduction

High-entropy alloys (HEAs) are defined as a kind of multi-component alloy materials containing at least five principal elements, and each one is in equal or near-equal atomic per cent ranging from 5 to 35 at.-% [1–5]. Compared to most of the intermetallic compounds with complex crystalline structures, HEAs (consisting of normally single- or dual-phase solid solutions) exhibit simple face-centered cubic (FCC) and/or body-centered cubic (BCC) structure [4]. Owing to the special multi-component feature, HEAs exhibit novel properties including high strength, high hardness, excellent thermal stability, and outstanding wear, corrosion and oxidation resistances, which can be used as advanced structure materials in many fields [6–9].

In order to realise practical applications of HEAs, their welding performance, including microstructural evolution during welding and mechanical properties after welding, needs to be well characterised. This topic has attracted growing interest in recent years [10–19], and two review articles on this topic have been published [20,21]. Some studies have been dedicated to fusion welding of HEAs based on various types of heat sources, such as gas tungsten arc [19,22], electron beam [12] and laser beam [10,11,23,24]. For gas tungsten arc welding, the welded $Al_{0.5}$CoCrFeNi HEA shows a clear drop in yield strength and ultimate tensile strength although high proportion of the ductility against the base metal (BM) can be maintained, and the microhardness in the fusion zone is lower than the BM [22]. For electron beam welding, there is an apparent grain growth in the fusion zone for CoCrFeMnNi HEA [12]. For laser beam welding, the welded $Al_{0.5}$CoCrFeNi also exhibits a decline in microhardness for the fusion zone although the fusion zone is clearly refined [23]. The decline is attributed to the decrease of the harder Al–Ni rich BCC phase. In another work [24], grains in the fusion zone are greatly coarsened after laser welding of $CoCrFeNiAl_{0.3}$ HEA, leading to a 60% reduction in microhardness of the fusion zone. It is found that fusion welding usually leads to coarsened grains [12,19] and may result in crack formation during solidification of fusion zone [25] for HEAs, which may cause a declined mechanical properties of the joint. The heat density of fusion welding is in the order of 10^5–10^8 W cm^{-2}, which is high enough for grains to grow [20]. It is reported that laser welding can refine grains in the fusion zone for the CrMnFeCoNi HEA in some cases [10,26], and it can generate a joint with mechanical properties comparable to the BM. However, a study clearly shows that the mechanical properties of the laser-welded joint are inferior to that of the friction stir welded one [17]. Friction stir welding (FSW) is one type of friction welding.

Generally, friction welding, as a solid-state welding method, can greatly refine the grains in the weld and thus can obtain a stronger bonding, which makes it a very promising method for welding HEAs

CONTACT Tao Zhang zhangtao@buaa.edu.cn Key Laboratory of Aerospace Materials and Performance (Ministry of Education), School of Materials Science and Engineering, Beihang University, Beijing 100191, People's Republic of China

Supplemental data for this article can be accessed here. https://doi.org/10.1080/13621718.2021.1957631

[20,21,27,28]. Friction welding has the advantages of high efficiency and grain refinement effect due to low heat accumulation compared to fusion welding. Currently, friction welding of HEAs is mainly focused on FSW [13–18]. During FSW, two pieces of materials are heavily deformed by a fast-rotating tool and then welded by recrystallisation as a result of the friction heat [13,29]. It is reported that a relative sound bonding of the $Co_{16}Fe_{28}Ni_{28}Cr_{28}$ alloy was achieved by FSW [14]. The stir zone remained a single FCC phase and exhibited a refined microstructure compared with the BM. FSW was also used as a processing method to enhance the mechanical properties of HEAs [15,16]. More recently, the $Al_{0.3}CoCrCu_{0.3}FeNi$ HEA was successfully butt welded by FSW [13]. The material in the stir zone demonstrates excellent transverse tensile properties and has overcome the common strength-ductility trade-off, which is attributed to its fine-grained and partially recrystallised microstructure. The advantages of FSW are obvious. But there are also certain shortcomings for FSW, which are mainly manifested in the following four aspects. First, FSW is primarily used on Al, a low melting point metal [27,30,31]. For metal materials with higher melting points such as steel, the weld thickness is limited to 25 mm or less [27]. Second, FSW is mainly used to weld plate workpieces, which must be rigidly fixed on a bottom plate [27,28]. Thirdly, the stir pin needs to be replaced regularly due to the occurrence of wear and the stir pin material may pollute the weld joint to form defects [32,33]. Finally, the compression of the shoulder during FSW causes a thinning phenomenon, which is a typical defect of FSW [34]. As a result, the stir zone becomes the initiation point of the crack and adversely affects the mechanical properties [34]. Based on the above analysis, it can be seen that it is of great significance to explore other friction welding methods. Direct drive friction welding (DDFW) is the most typical friction welding method, which has been in commercial use since the 1940s [28]. DDFW can be used to join a wide range of metal materials like Al alloy, Mg alloy, steel, superalloy, etc., without strict limitation on the size of the workpiece to be welded [27,28]. DDFW requires a constant energy input. During the DDFW process, one workpiece is rotated and the other is held fixedly when the two workpieces are moved together and an axial force is applied [27]. DDFW has the potential to become an ideal welding method with low cost, high efficiency and quality for joining HEAs.

In this paper, a quinary $Al_{13}Cr_{23.5}Fe_{20}Co_{20}Ni_{23.5}$ HEA with excellent comprehensive mechanical properties was selected for DDFW [35]. The selected $Al_{13}Cr_{23.5}Fe_{20}Co_{20}Ni_{23.5}$ HEA is based on the Al–Cr–Fe–Co–Ni HEA system, which is a typical system for HEAs [36,37]. The microstructure and various properties (like mechanical, corrosion, thermophysical, electrical, etc.) of the HEA system have been well studied, showing great potential to be used in practical applications [3,15,35,37–41]. The specific composition is obtained by optimising the concentrations of Al, Cr and Ni simultaneously in the equimolar AlCrFeCoNi HEA [35]. More importantly, the $Al_{13}Cr_{23.5}Fe_{20}Co_{20}Ni_{23.5}$ HEA possesses three phases. Thus, it is very suitable for analysing the thermal-mechanical effects on the phase evolution during the DDFW process. Tensile mechanical properties of the welded samples were evaluated. Morphologies of the failed samples were observed. The distribution of microhardness of the weld joint was measured and related with the microstructural evolution across the weld interface. The microstructure of the weld joint was observed by scanning electron microscopy (SEM) and transmission electron microscopy (TEM).

Experimental

Ingots with a nominal chemical composition of $Al_{13}Cr_{23.5}Fe_{20}Co_{20}Ni_{23.5}$ (at.-%) were prepared by arc-melting mixtures of Al, Cr, Fe, Co and Ni metals ($>$ 99.9 wt-% purity) under a Ti-gettered Ar atmosphere. From the master alloys, HEA rods with a diameter of 6 mm were produced by a copper-mold casting method under an Ar atmosphere. DDFW was performed using a conventional friction welding machine (HL-8) in the air. A pair of machined specimens were welded at a rotation rate of 2000 rpm. The friction pressure and upsetting pressure were fixed at 100 MPa. The upsetting time was fixed as 3 s. Parameters of rotation rate, friction pressure, upsetting pressure and upsetting time were selected by referring to other literatures [42–49] and the mechanical properties of the as-cast HEA. Parameter optimisation was carried out only for friction time at 2, 4, 6 and 8 s.

Constituent phases of the HEA samples were identified by X-ray diffraction (XRD, Bruker D8-advance) with Co–Kα radiation. Microstructure of the as-cast, welded and failed samples was observed by SEM (JSM JOEL-7500F) with an X-ray energy dispersive spectroscopy (EDS) detector and TEM (JEOL-2100F). Volume fractions of constituent phases were evaluated by the digitised back-scattered electron (BSE) image by the software of ImageJ. Tensile tests were performed using an Instron 5500 universal testing machine at a strain rate of 1×10^{-3} s^{-1} at room temperature. The tensile samples with a gauge length of 15 mm and a diameter of 4 mm were cut carefully from the welded samples to ensure that the weld zone is perpendicular to the loading axis. The as-cast HEA rods were also measured under the same tensile conditions for comparison. Microhardness test was carried out by a Vickers hardness tester (450-SVD) under a load of 0.98 N applied for 15 s.

Results and discussion

Tensile mechanical properties of the as-cast and welded HEA samples with different friction times from 2 to 8 s were evaluated (Table 1). The corresponding true tensile strain–stress curves are shown in Figure S1. It can be seen that the $Al_{13}Cr_{23.5}Fe_{20}Co_{20}Ni_{23.5}$ HEA shows an obvious work-hardening effect and the effect is retained after DDFW. It also can be seen that the strength and elongation of the welded samples both increase with the prolongation of the friction time until they reach the maximum at 6 s. The microstructures of the weld joint for friction times of 2 and 4 s are shown in Figure S2. For the friction time of 2 s, a clear weld interface is detected, and the deformation in the weld is low. For the friction time of 4 s, the weld interface can still be identified although it is not very obvious. Besides, the degree of deformation increases. The weld interface disappears and the deformation further increases when the friction time is extended to 6 s, which will be shown below. It means that 6 s is a critical friction time to generate sufficient heat for sound bonding. As the friction time further increases, the mechanical properties of the welded samples remain almost unchanged, but slightly decrease. It is supposed that the slight decrease is attributed to grain coarsening resulting from excessive heat release. However, grain coarsening may be so minor that we do not recognise it in the microstructure. Besides, it can be seen that the welded samples with friction time of 6 s show strength and plasticity comparable to the as-cast ones, indicating that tensile mechanical properties of the welded $Al_{13}Cr_{23.5}Fe_{20}Co_{20}Ni_{23.5}$ HEA samples can be regenerated under optimal friction time of 6 s by DDFW. These results demonstrate that DDFW is a feasible method for welding HEAs. After a sound bonding is achieved, no further optimisation is conducted, and the work is to focus on revealing the relationships between the microstructural and mechanical evolution based on the sound joint.

Figure 1 shows the morphologies of the as-cast HEA sample and the welded one at an optimal friction time of 6 s after tensile fracture. As shown in Figure 1(a), the fracture surface of the as-cast HEA features a typical 'cup and cone' morphology consisting of fibrous zone, radial zone and shear lip. The fracture mode of the as-cast samples can be explained as follows. First, micro-holes are generated in the central part. Then, these micro-holes grow and accumulate to form a jagged fibrous fracture surface (fibrous zone). As the fibrous zone reaches a critical size, primary cracks propagate rapidly to form a radial zone. When the formation of the radial zone is completed, only the outermost ring is left as the area under load, and a shear lip forms caused by shear fracture finally. It can be inferred that it fractures from the central part for the as-cast sample. However, for the welded sample, micro-cracks normally initiate at the surface (as shown by the arrow in Figure 1(b)), resulting in a totally different fracture surface pattern. For DDFW, more heat is generated in the periphery region than the central region due to the higher friction speed in the periphery region. Excessive heat may result in a larger grain size in the periphery region, which may be responsible for the initiation of micro-cracks at the surface for the welded HEA samples. Figure 1(c,d) is the magnified SEM image of the fracture surfaces marked by rectangles in Figure 1(a,b), respectively. It can be seen that the fracture surface of the welded sample is smoother than that of the as-cast one, but the two fracture surfaces both show a typical dimple pattern. It means that the weld joint still shows a certain degree of ductility.

Table 1. Tensile mechanical properties of the as-cast HEA samples and the welded ones with different friction times.

Friction time (s)	Yield strength (MPa)	Fracture strength (MPa)	Uniform elongation (%)
2	316 ± 56	680 ± 57	3.1 ± 6.7
4	397 ± 37	951 ± 45	9.9 ± 3.8
6	431 ± 35	1024 ± 33	13.4 ± 3.2
8	426 ± 25	1008 ± 36	12.5 ± 5.1
As-cast	442 ± 34	1031 ± 27	13.8 ± 2.2

Apart from tensile tests, microhardness distribution across the weld interface was measured for samples welded at an optimal friction time of 6 s. As shown in Figure 2, the microhardness increases gradually from $\sim$ 331 HV in the substrate to $\sim$ 382 HV near the weld interface. The results indicate that the thermo-mechanical processing of DDFW can introduce an obvious hardening effect in the weld joint for the HEA. Besides, it can be seen that microhardness distribution is very symmetrical about the weld interface, which differs from the case for FSW. It is reported that the advancing side has a finer grain size than the retreating side [15], leading to an asymmetrical hardness distribution curve.

The microhardness distribution should be related to the microstructural evolution across the weld interface. Figure 3(a) shows a BSE image of the joint for a typical HEA sample friction-welded for 6 s. Two kinds of phases denoted as dark phase and grey phase (marked in Figure 3(d)) can be observed in the whole samples. The elemental concentrations of the two phases and the HEA alloy were determined by EDS analysis, and the data are listed in Table 2. Compared to the average chemical composition of the HEA alloy, the dark phase is Al-rich while the grey phase is Al-poor. According to the microstructural characteristics, the joint can be divided into four regions, i.e. dynamic recrystallisation zone (DRZ), thermal-mechanically affected zone (TMAZ), heat-affected zone (HAZ) and BM. Accordingly, four regions are identified in the microhardness profile, as shown in Figure 2. It can be seen that the microhardness distribution agrees very well with the microstructural evolution across the weld interface.

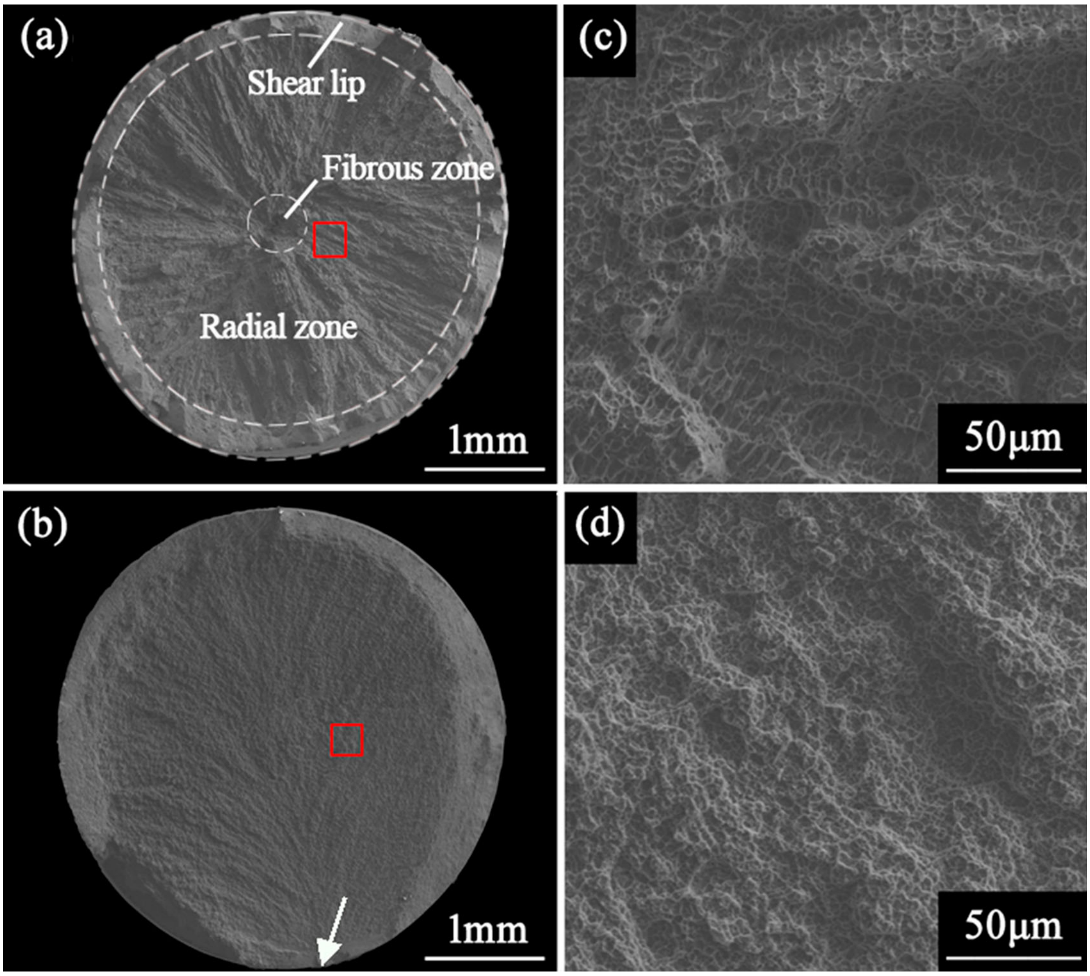

Figure 1. Typical morphologies after tensile failure for (a) the as-cast HEA sample and (b) the welded one with the optimal friction time of 6 s. (c) and (d) are the magnified images of the fracture surfaces marked by the rectangles in (a) and (b), respectively.

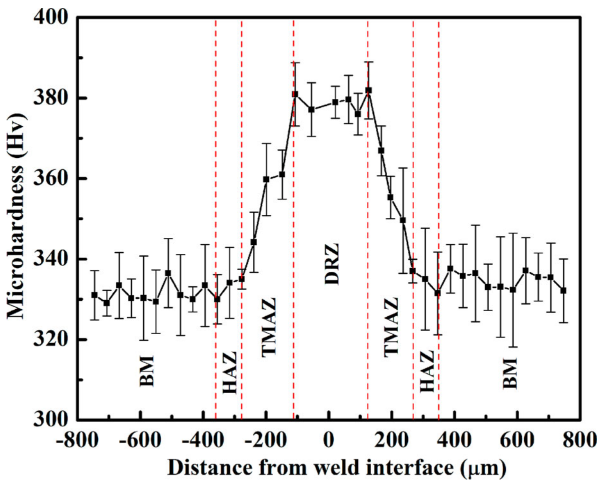

Figure 2. Distribution of microhardness across the weld interface for the welded samples with the optimal friction time of 6 s.

Figure 3(b–d) shows the magnified BSE images of DRZ, TMAZ and HAZ, respectively. The DRZ is composed of equiaxed grains, which is totally different from the dendrite structure of BM. In DRZ, a refined microstructure is detected, which greatly contributes to the high microhardness of this region. In this region, the plastic strain is accommodated by dynamic recrystallisation and thus no deformed grains can be seen (Figure 3(b)) [27]. In TMAZ, the grains are elongated and flattened, indicating the happening of a heavy plastic deformation. In this zone, the degree of plastic deformation is accommodated by an increase in the dislocation density of the matrix grains [27], which further improves the microhardness of this region especially for the present alloy with a work-hardening effect. In TMAZ, the degree of deformation decreases as approaching HAZ, which to some extent is responsible for the microhardness change in this region. HAZ is an undeformed zone, where the microhardness is similar to BM. Long and large-size dendrite grey phases that can be easily detected in BM are seldom seen in HAZ, suggesting that phase transformation occurs in HAZ due to heat effect during friction welding. In addition, it can be seen that there is no detectable grain growth in HAZ. It is well known that intense atomic diffusion is required to complete the migration of grain boundaries for grain growth [50]. However, atomic diffusion is greatly hindered by the low temperature in HAZ and the sluggish diffusion in HEA [1,7], leading to an insignificant grain growth.

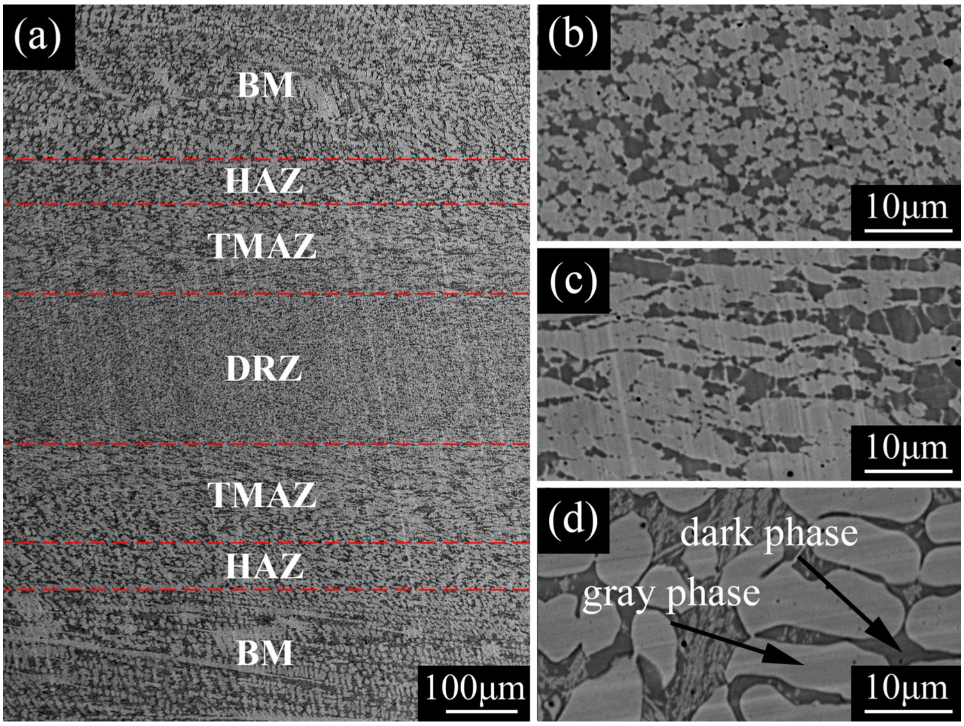

Figure 3. (a) BSE image of the weld joint for the HEA with the optimal friction time of 6 s. (b), (c) and (d) are locally magnified images in DRZ, TMAZ and HAZ, respectively.

Table 2. Compositions of the constituent phases and the average composition of the HEA.

Phase	Al (at.-%)	Cr (at.-%)	Fe (at.-%)	Co (at.-%)	Ni (at.-%)
Dark phase	17.28	21.13	17.47	19.19	24.93
Grey phase	9.12	24.14	21.78	21.39	23.57
HEA	12.57	22.86	20.16	19.71	24.70

TEM was conducted to determine the crystal structures of the dark and grey phases shown in Figure 3. Figure 4(a) shows the bright-field TEM image of the DRZ for the welded HEA sample. TEM results show that DRZ consists of three phases, instead of two phases identified by the BSE image. As inferred from the selected-area electron diffraction (SAED) patterns shown in Figure 4(b), the region in the lower-left corner in Figure 4(a) shows the FCC structure. As clearly revealed by Figure 4(c–f), the region in the top-right corner of Figure 4(a) features a A2+B2 two-phase structure (A2 denotes the disordered BCC structure, B2 denotes one type of the ordered BCC structure). As an intermetallic compound, the B2 phase is precipitated from the A2 matrix due to a spinodal decomposition during the cooling of the HEA [51]. Actually, the other three regions (TMAZ, HAZ and BM) for the welded HEA are also composed of FCC, A2 and B2 phases, which means that the thermal-mechanical effects of DDFW will not render the disappearance of constituent phases. Phase compositions were characterised again by EDS in TEM. The FCC phase is the Al-poor one with a nominal composition of $Al_{8.40}Cr_{24.60}Fe_{20.90}Co_{20.30}Ni_{25.80}$ (at.-%), while the BCC phases (A2+B2) are Al-rich ones with an average nominal composition of $Al_{18.20}Cr_{19.60}Fe_{16.30}Co_{18.20}Ni_{27.70}$ (at.-%). Thus, it can be deduced that the dark phase and the grey phase shown in Figure 3 feature BCC (A2+B2) structure and FCC structure, respectively.

In order to investigate the influence of the thermo-mechanical processing of DDFW on the phase transformation in the weld joint, the volume fractions of the FCC and BCC (A2+B2) phases in different regions were evaluated based on the digitised BSE image by the software of ImageJ. First, the BSE image was converted to greyscale one. Second, a greyscale threshold was determined according to the greyscale values of the BCC and FCC phases. Finally, the volume fractions of BCC and FCC phases were measured based on that the proportion of the area whose greyscale value is lower/higher than the threshold corresponds to the volume fraction of the BCC/FCC phase, respectively. Six BSE images are analysed to obtain the mean value and error bars. As shown in Figure 5, from BM to HAZ, the volume fractions of the FCC and BCC (A2+B2) phases change very little, which could explain the similar hardness between HAZ and BM. However, from HAZ to DRZ, the volume fraction of the BCC (A2+B2) phases increases while the volume fraction of the FCC phase decreases. Correspondingly, the volume fraction ratio of FCC to BCC (A2+B2) phases decreases from 1.82 to 1.52. It is concluded that the thermo-mechanical processing of DDFW can induce a phase transformation from FCC to BCC in the weld joint. The increase in volume fraction of the BCC (A2+B2) phases can

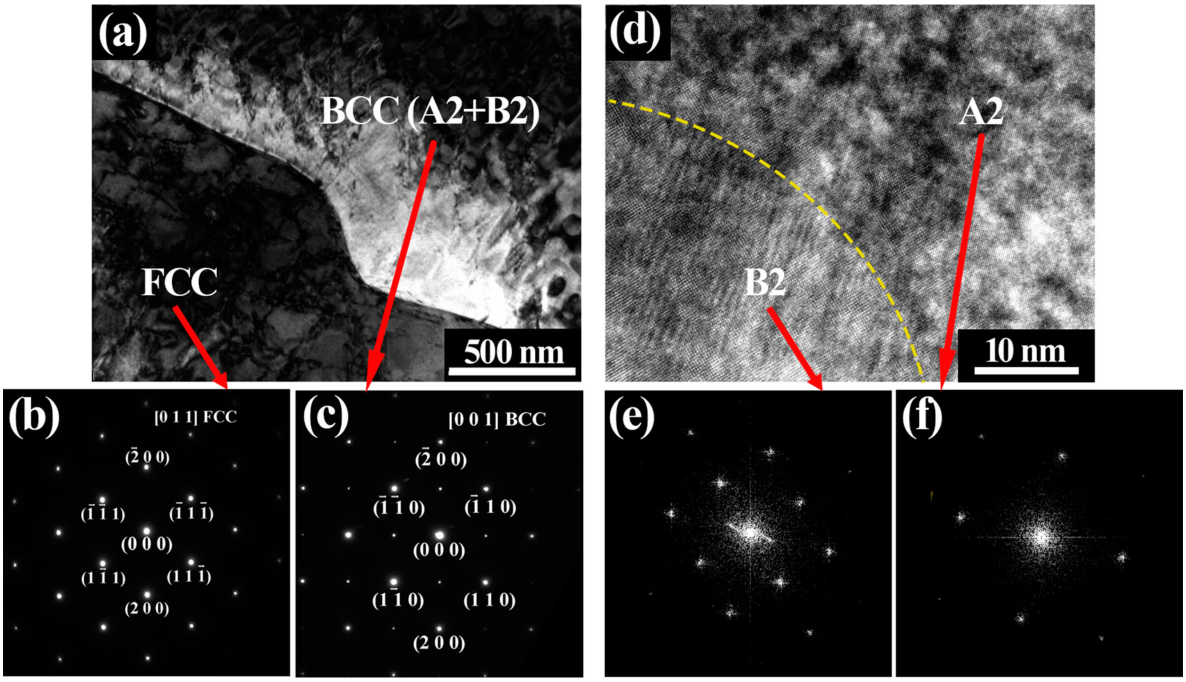

Figure 4. (a) Bright-field TEM image of the welded HEA sample in DRZ. (b) and (c) are the SAED patterns for the lower-left and top-right corner of (a), respectively. (d) High-resolution TEM image located in the top-right corner of (a), where the interface between the precipitated B2 and the substrate A2 phases can be clearly seen. (e) and (f) are the fast Fourier transform spot patterns of the B2 and A2 phases, respectively.

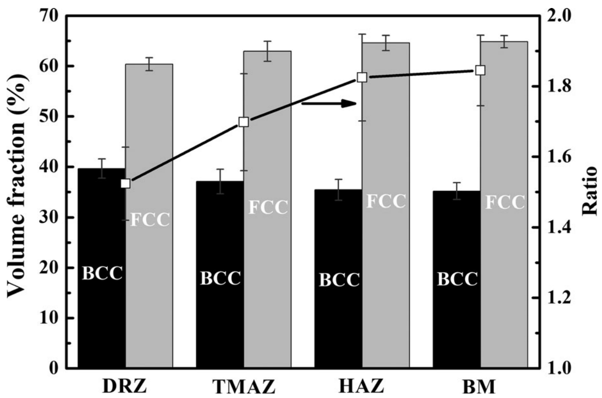

Figure 5. Volume fractions of the BCC (A2+B2) and FCC phases (bar graph) as well as the volume fraction ratio of FCC to BCC (A2+B2) phases (line + square graph) in different regions for the welded samples with a friction time of 6 s.

contribute to the increase of microhardness in the weld joint because the BCC phase is harder than the FCC phase [38].

In summary, a sound bonding was achieved for $Al_{13}Cr_{23.5}Fe_{20}Co_{20}Ni_{23.5}$ HEA by DDFW. The tensile properties of the welded HEA specimens at optimal friction time are comparable to that of the as-cast ones. The microhardness distribution across the weld interface was studied and the results indicate that the thermo-mechanical processing of DDFW can distinctly harden the weld joint. The microstructure evolution in the weld joint was further studied, which agrees well with the microhardness distribution. The thermo-mechanical processing of DDFW can induce a phase transformation from FCC to BCC in the weld joint.

Conclusions

(1) The direct drive friction welded HEA specimens demonstrate excellent tensile mechanical properties (yield strength: 431 ± 35 MPa; fracture strength: 1024 ± 33 MPa; uniform elongation: $13.4 \pm 3.2\%$), which are very close to that of the as-cast ones (yield strength: 442 ± 34 MPa; fracture strength: 1031 ± 27 MPa; uniform elongation: $13.8 \pm 2.2\%$).

(2) The microhardness increases gradually from ~ 331 HV in the BM to ~ 382 HV near the weld interface, indicating that a hardened joint is obtained.

(3) The joint can be divided into four regions: DRZ, TMAZ, HAZ and BM. The four regions all consist of three phases: FCC phase, A2 phase and B2 phase precipitated from the A2 phase. The thermal-mechanical effects of DDFW do not render the disappearance of the constituent phases. But the volume fraction ratio of FCC to BCC phases decreases from 1.82 to 1.52 as approaching the weld interface.

(4) The microstructural evolution agrees well with the microhardness distribution in the weld joint. The hardened joint is derived from the refined microstructure, large deformation and increase in the volume fraction of the harder BCC phases.

Disclosure statement

No potential conflict of interest was reported by the author(s).

Funding

This work was supported by China Postdoctoral Science Foundation [Grant Number 2020M680014].

References

[1] Yeh JW, Chen SK, Lin SJ, et al. Nanostructured high-entropy alloys with multiple principal elements: novel alloy design concepts and outcomes. Adv Eng Mater. 2004;6(5):299–303.
[2] Sathiaraj GD, Ahmed MZ, Bhattacharjee PP. Microstructure and texture of heavily cold-rolled and annealed fcc equiatomic medium to high entropy alloys. J Alloy Compd. 2016;664:109–119.
[3] Li DY, Li CX, Feng T, et al. High-entropy $Al_{0.3}CoCrFeNi$ alloy fibers with high tensile strength and ductility at ambient and cryogenic temperatures. Acta Mater. 2017;123:285–294.
[4] Tsai MH, Yeh JW. High-entropy alloys: a critical review. Mater Res Lett. 2014;2(3):107–123.
[5] Zhang Y, Zhou YJ, Lin JP, et al. Solid-solution phase formation rules for multi-component alloys. Adv Eng Mater. 2008;10(6):534–538.
[6] Yao YG, Huang ZN, Xie P, et al. Carbothermal shock synthesis of high-entropy-alloy nanoparticles. Science. 2018;359:1489–1494.
[7] Tsai KY, Tsai MH, Yeh JW. Sluggish diffusion in Co-Cr-Fe-Mn-Ni high-entropy alloys. Acta Mater. 2013;61(13):4887–4897.
[8] Zhang Y, Yang X, Liaw PK. Alloy design and properties optimization of high-entropy alloys. JOM. 2012;64(7): 830–838.
[9] Shuang S, Ding ZY, Chung D, et al. Corrosion resistant nanostructured eutectic high entropy alloy. Corros Sci. 2020;164:108315.
[10] Chen Z, Wang BF, Duan BH, et al. Mechanical properties and microstructure of laser welded FeCoNiCrMn high-entropy alloy. Mater Lett. 2020;262:127060.
[11] Nam H, Park S, Chun EJ, et al. Laser dissimilar weldability of cast and rolled CoCrFeMnNi high-entropy alloys for cryogenic applications. Sci Technol Weld Joining. 2020;25(2):127–134.
[12] Wu Z, David SA, Leonard DN, et al. Microstructures and mechanical properties of a welded CoCrFeMnNi high-entropy alloy. Sci Technol Weld Joining. 2018;23(7):585–595.
[13] Lin PT, Liu HC, Hsieh PY, et al. Heterogeneous structure-induced strength-ductility synergy by partial recrystallization during friction stir welding of a high-entropy alloy. Mater Des. 2021;197:109238.
[14] Zhu ZG, Sun YF, Ng FL, et al. Friction-stir welding of a ductile high entropy alloy: microstructural evolution and weld strength. Mater Sci Eng A. 2018;711:524–532.
[15] Komarasamy M, Kumar N, Tang Z, et al. Effect of microstructure on the deformation mechanism of friction stir-processed $Al_{0.1}CoCrFeNi$ high entropy alloy. Mater Res Lett. 2014;3(1):30–34.
[16] Kumar N, Komarasamy M, Nelaturu P, et al. Friction stir processing of a high entropy alloy $Al_{0.1}CoCrFeNi$. JOM. 2015;67(5):1007–1013.
[17] Jo MG, Kim HJ, Kang M, et al. Microstructure and mechanical properties of friction stir welded and laser welded high entropy alloy CrMnFeCoNi. Met Mater Int. 2018;24(1):73–83.
[18] Shaysultanov D, Stepanov N, Malopheyev S, et al. Friction stir welding of a carbon-doped CoCrFeNiMn high-entropy alloy. Mater Charact. 2018;145:353–361.
[19] Oliveira JP, Curado TM, Zeng Z, et al. Gas tungsten arc welding of as-rolled CrMnFeCoNi high entropy alloy. Mater Des. 2020;189:108505.
[20] Guo J, Tang C, Rothwell G, et al. Welding of high entropy alloys-a review. Entropy (Basel). 2019;21(4): 431.
[21] Lopes JG, Oliveira JP. A short review on welding and joining of high entropy alloys. Metals (Basel). 2020;10(2):212.
[22] Sokkalingam R, Mishra S, Cheethirala SR, et al. Enhanced relative slip distance in gas-tungsten-arc-welded $Al_{0.5}CoCrFeNi$ high-entropy alloy. Metall Mater Trans A. 2017;48(8):3630–3634.
[23] Sokkalingam R, Sivaprasad K, Muthupandi V, et al. Characterization of laser beam welded $Al_{0.5}CoCrFeNi$ high-entropy alloy. Key Eng Mater. 2018;775:448–453.
[24] Chen SJ, Liu Q, He TB, et al. Inhomogeneity of microstructure and mechanics of laser welded $CoCrFeNiAl_{0.3}$ high entropy alloy. Mater Lett. 2021;301: 130269.
[25] Nahmany M, Hooper Z, Stern A, et al. $Al_xCrFeCoNi$ high-entropy alloys: surface modification by electron beam bead-on-plate melting. metallography. Microstruct Anal. 2016;5(3):229–240.
[26] Kashaev N, Ventzke V, Petrov N, et al. Fatigue behaviour of a laser beam welded CoCrFeNiMn-type high entropy alloy. Mater Sci Eng A. 2019;766:138358.
[27] Uday MB, Ahmad Fauzi MN, Zuhailawati H, et al. Advances in friction welding process: a review. Sci Technol Weld Joining. 2010;15(7):534–558.
[28] Maalekian M. Friction welding - critical assessment of literature. Sci Technol Weld Joining. 2013;12(8): 738–759.
[29] Mishra RS, Ma ZY. Friction stir welding and processing. Mater Sci Eng R. 2005;50(1-2):1–78.
[30] Buchibabu V, Reddy GM, De A. Probing torque, traverse force and tool durability in friction stir welding of aluminum alloys. J Mater Process Technol. 2017;241:86–92.
[31] Buchibabu V, Reddy GM, Kulkarni D, et al. Friction stir welding of a thick Al-Zn-Mg alloy plate. J Mater Eng Perform. 2016;25(3):1163–1171.
[32] Buchibabu V, Lemos GVB, Bergmann L, et al. Probing underlying mechanisms for PCBN tool decay during friction stir welding of nickel-based alloys. Tecnol Metal Mater Min. 2021;18:e2455.
[33] Buchibabu V, Liu HH, Morisada Y, et al. Degradation of nickel-bonded tungsten carbide tools in friction stir welding of high carbon steel. Int J Adv Manuf Technol. 2021;115(4):1049–1061.
[34] Park S, Park C, Na Y, et al. Effects of (W, Cr) carbide on grain refinement and mechanical properties for CoCrFeMnNi high entropy alloys. J Alloy Compd. 2019;770:222–228.
[35] Chen C, Pang SJ, Cheng YY, et al. Microstructure and mechanical properties of $Al_{20-x}Cr_{20+0.5x}Fe_{20}Co_{20}Ni_{20+0.5x}$ high entropy alloys. J Alloy Compd. 2016;659: 279–287.
[36] Miracle DB, Senkov ON. A critical review of high entropy alloys and related concepts. Acta Mater. 2017;122:448–511.

[37] Lin CM, Tsai HL. Evolution of microstructure, hardness, and corrosion properties of high-entropy $Al_{0.5}$ CoCrFeNi alloy. Intermetallics. 2011;19(3):288–294.
[38] Kao YF, Chen TJ, Chen SK, et al. Microstructure and mechanical property of as-cast, -homogenized, and -deformed Al_xCoCrFeNi ($0 \le x \le 2$) high-entropy alloys. J Alloy Compd. 2009;488(1):57–64.
[39] Wang WR, Wang WL, Wang SC, et al. Effects of Al addition on the microstructure and mechanical property of Al_xCoCrFeNi high-entropy alloys. Intermetallics. 2012;26:44–51.
[40] Wang YP, Li BS, Ren MX, et al. Microstructure and compressive properties of AlCrFeCoNi high entropy alloy. Mater Sci Eng A. 2008;491(1-2):154–158.
[41] Chou H-P, Chang Y-S, Chen S-K, et al. Microstructure, thermophysical and electrical properties in Al_x CoCrFeNi ($0 \le x \le 2$) high-entropy alloys. Mater Sci Eng B. 2009;163(3):184–189.
[42] Nguyen TC, Weckman DC. A thermal and microstructure evolution model of direct-drive friction welding of plain carbon steel. Metall Mater Trans B. 2006;37B:275–282.
[43] Sathiya P, Aravindan S, Noorul Haq A. Effect of friction welding parameters on mechanical and metallurgical properties of ferritic stainless steel. Int J Adv Manuf Technol. 2006;31(11-12):1076–1082.
[44] Sahin M, Akata HE, Gulmez T. Characterization of mechanical properties in AISI 1040 parts welded by friction welding. Mater Charact. 2007;58(10):1033–1038.
[45] Reddy G M, Rao K S. Microstructure and mechanical properties of similar and dissimilar stainless steel electron beam and friction welds. Int J Adv Manuf Technol. 2009;45(9-10):875–888.
[46] Huang ZW, Li HY, Baxter G, et al. Electron microscopy characterization of the weld line zones of an inertia friction welded superalloy. J Mater Process Technol. 2011;211(12):1927–1936.
[47] Kimura M, Kusaka M, Seo K, et al. Properties and improvement of super fine grained steel friction welded joint. Sci Technol Weld Joining. 2013;11(4):448–454.
[48] Nie LF, Zhang LW, Zhu Z, et al. Microstructure evolution modeling of FGH96 superalloy during inertia friction welding process. Finite Elem Anal Des. 2014;80:63–68.
[49] Wang FF, Li WY, Li JL, et al. Process parameter analysis of inertia friction welding nickel-based superalloy. Int J Adv Manuf Technol. 2014;71(9-12):1909–1918.
[50] Fukuda Y, Kado Y, Yoshikawa T, et al. Diffusion distances of the constituent atoms in the metallurgical phenomena such as recovery, recrystallization, grain growth, and aging in aluminum and copper alloys. J Mater Eng Perform. 2002;11(5):544–550.
[51] Tung CC, Yeh JW, Tt S, et al. On the elemental effect of AlCoCrCuFeNi high-entropy alloy system. Mater Lett. 2007;61(1):1–5.